INTERNATIONAL JOURNAL FOR NUMERICAL METHODS IN FLUIDS, VOL. 15, 329–354 (1992)

FLUID FLOW AND HEAT TRANSFER TEST PROBLEMS FOR NON-ORTHOGONAL GRIDS: BENCH-MARK SOLUTIONS

I. DEMIRDŽIĆ

Mašinski fakultet, Omladinsko šetalište bb, 71000 Sarajevo, Bosnia-Herzegovina

AND

Ž. LILEK AND M. PERIĆ

Lehrstuhl für Strömungsmechanik, Cauerstrasse 4, D-8520 Erlangen, Germany

SUMMARY

Four problems of fluid flow and heat transfer were designed in which non-orthogonal, boundary-fitted grids were to be used. These are proposed to serve as test cases for testing new solution methods. This paper presents solutions of the test problems obtained by using a multigrid finite volume method with grids of up to 320×320 control volumes. Starting from zero fields, iterations were performed until the sum of the absolute residuals had fallen seven orders of magnitude, thus ensuring that the variable values did not change to six most significant digits. By comparing the solutions for successive grids at moderate Reynolds and Rayleigh numbers, the discretization errors were estimated to be lower than 0·1%. The results presented in this paper may thus serve for comparison purposes as bench-mark solutions.

KEY WORDS Finite volume Multigrid Non-orthogonal grid Numerical accuracy Bench-mark solutions

1. INTRODUCTION

International journals for the numerical treatment of fluid flow and heat transfer problems are publishing more and more papers describing new solution methods based on boundary-fitted, non-orthogonal grids. The evaluation of the new methods is very difficult for an observer, since the common criteria and test cases are missing. The situation is much clearer in the case of the methods for orthogonal grids: several well-established test cases with bench-mark solutions are available in the literature, e.g. lid-driven cavity flow,[1] buoyancy-driven cavity flow,[2, 3] etc.

For a potential user wishing to adopt one of the new methods, the essential criteria are: (i) accuracy of the method and (ii) computational effort at a given grid fineness. Both criteria are difficult to define precisely; however, a rough estimate is always possible if the methods are applied to the same test problem and if accurate reference solutions are available. Unfortunately, such reference solutions for non-orthogonal geometries could not be found in the literature at the present time.

The aim of the present paper is to present four test problems for fluid flow and heat transfer calculation using non-orthogonal grids and provide accurate reference solutions which can be used for comparison purposes. These four test cases are described in detail in Section 2. To solve

0271–2091/92/150329–26$18.00

Received October 1991
Revised February 1992

them, a multigrid finite volume solution method was employed. The single-grid version of the method is described by Demirdžić and Perić;[4] the multigrid algorithm is described in conjunction with Cartesian grids by Hortmann *et al.*[3] For this reason, only a short description of the solution method has been given.

The conservation equations for mass, momentum and temperature are discretized on non-orthogonal grids using the finite volume approach and a collocated arrangement of variables.[5] The equations are solved sequentially using the strongly implicit procedure of Stone,[6] which is based on the ILU-decomposition. Pressure–velocity coupling is achieved via the SIMPLE algorithm.[7] The cross-derivatives resulting from non-orthogonality are treated explicitly,[8] except in the pressure-correction equation, where implicit treatment is necessary at severe non-orthogonality.[9] Central differences are used to approximate both convection and diffusion fluxes. For convection terms, the deferred-correction approach was used.[10] Grid refinement is performed systematically by subdividing one coarse-grid control volume (CV) into four fine-grid CVs and so on. The multigrid procedure is based on V-cycles and the full approximation scheme. It is implemented as a full-multigrid algorithm, i.e. first the solution on the coarsest grid is obtained; then it is extrapolated to the next finer grid where it serves as the initial field for the two-grid V-cycles. The same procedure is repeated until the finest grid is reached. In this way, converged solutions on all grids employed in the solution process are obtained. They are used to evaluate the discretization accuracy, since the difference between two solutions on consecutive grids is proportional to the error on the finer grid.[11]

In Section 2, the four test problems are defined. The results of the calculations and their discussion are presented in Section 3. Finally, some conclusions from the present calculations are drawn.

2. DESCRIPTION OF THE TEST CASES

The problems defined below are chosen so as to include the most important features of the complex flows encountered in engineering practice and also to provide good tests for the solution methods. The first three cases involve a quadrilateral solution domain with parallel walls at different inclinations. The obvious choice of numerical grid is to let the grid lines be parallel to the domain boundaries leading to uniform grid non-orthogonality. Since the grid non-orthogonality is one of the limiting parameters in many solution methods, the angles of 45° and 30° were chosen.

The fourth test case involves domain geometry which requires non-uniform, non-orthogonal grids with variable aspect ratio and non-orthogonality (90°–45°). As far as grid non-orthogonality is concerned, these four cases are likely to cover all of the relevant effects. The first two test cases involve laminar flows in which the fluid motion is induced by the movement of one wall (lid-driven cavity flows). In the last two cases, the fluid flow is induced by buoyancy, and an equation for temperature needs to be solved as well.

Various kinds of boundary conditions are also involved: specified boundary values (wall velocity or temperature), symmetry conditions and adiabatic walls. From this point of view, the test cases can be seen as being representative of a wide class of problems. At moderate Reynolds and Rayleigh numbers, the coupling of the variables U, V, P and T is sufficient to test the efficiency of the solution method. The individual test cases with the appropriate boundary conditions are defined below.

2.1. Test cases C1 and C2

Lid-driven cavity flow has long served as a standard test case for orthogonal grids.[1] Appropriate test cases for non-orthogonal grids can be set up by inclining the side walls or by squeezing the

cavity (cf. Figure 1). Test case C1 corresponds to the angle $\beta = 45°$, and test case C2 corresponds to $\beta = 30°$. In both cases, $L = 1$, density $\rho = 1$ and lid velocity $U_L = 1$ were used in the calculations. The Reynolds number, defined using the lid velocity, U_L, and cavity length, L, was varied from 100 to 1000 by changing the viscosity from 0·01 to 0·001.

2.2. *Test case C3*

Buoyancy-driven cavity flow has also been a popular test case for heat transfer calculations on orthogonal grids.[2, 3] An appropriate test case for a non-orthogonal grid is designed by squeezing the cavity, as in cases C1 and C2 (cf. Figure 2). The inclined walls are kept at constant temperatures T_H and T_C, respectively, while the horizontal walls are assumed adiabatic. The inclination angle was chosen to be $\beta = 45°$. Gravity acts in the vertical direction. The dimensions

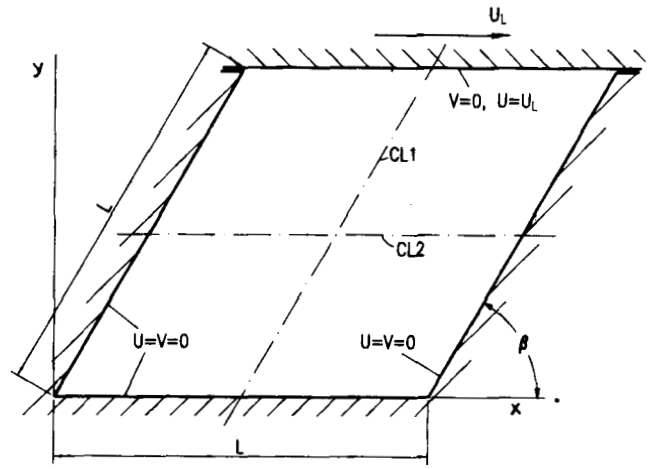

Figure 1. Geometry and boundary conditions for test cases C1 and C2

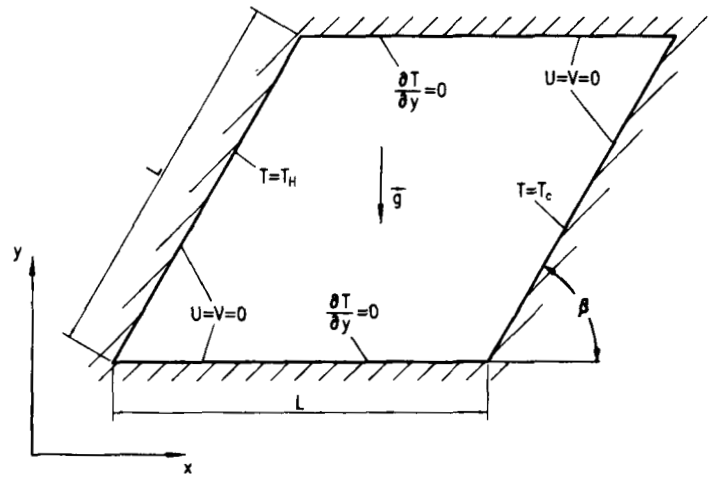

Figure 2. Geometry and boundary conditions for test case C3

and fluid properties used were: $L=1$, $\rho=1$, gravity constant $g=1$, expansion coefficient $\beta=0{\cdot}1$, specific heat $C_p=1$, $T_H=1$ and $T_C=0$, so that the Rayleigh number is only a function of the viscosity and the Prandtl number:

$$Ra=\frac{\rho^2 g\beta L^3\Delta T}{\mu^2}Pr=\frac{0{\cdot}1}{\mu^2}Pr.$$

Flows at $Ra=10^6$ were studied for two values of the Prandtl number: $Pr=0{\cdot}1$ and 10, corresponding to $\mu=10^{-4}$ and 10^{-3}, respectively.

2.3. Test case C4

Heat transfer between concentric cylinders, both symmetrically and asymmetrically arranged, was often a subject for experimental and numerical heat transfer studies.[12] Here, a similar test case is proposed, namely the heat transfer from a cylinder whose wall is maintained at a constant temperature $T_H=1$ and which is enclosed by a square duct. The vertical duct walls are kept at a lower temperature $T_C=0$ (cf. Figure 3). The horizontal duct walls are assumed adiabatic. Gravity acts in the vertical direction. Only one-half of the geometry is considered due to the existence of a vertical plane of symmetry. The cylinder centre is displaced from the duct centre vertically for $\Delta y_C=0{\cdot}1$; its radius is $R=0{\cdot}2$, and the duct dimensions are $L=H=1$. Fluid properties were as in case C3; also, the values for $T_H=1$ and $T_C=0$ were the same, yielding a Rayleigh number of 10^6 based on the duct width.

3. RESULTS AND DISCUSSION

Assuming that the conservative equations for mass, momentum and energy (temperature), as given e.g. by Hortmann *et al.*,[3] describe the laminar flow and heat transfer accurately and that the Boussinesq approximation is valid, the numerical solutions are affected only by the following errors:*

(i) discretization errors (the difference between the exact solution of the correctly discretized equations on a given grid and the exact solution of the governing differential equations)
(ii) convergence errors (the difference between the exact and the approximate solution of the discretized equations left over after stopping the iterations)
(iii) algorithmic and programming errors (errors due to incorrect discretization, erroneous implementation of boundary conditions and programming errors, etc.).

The third type of error, although common in practice, will be assumed to be absent here. Extensive tests of the computer code during the past five years justify this assumption, although we cannot offer any definite proof that such errors do not really exist.

The second type of error was minimized in our calculations by iterating long enough for the variable values to be accurate to six most significant digits. Calculations were always started from zero fields. After each iteration, the sum of the absolute values of the residuals in all control volumes was calculated for each variable. These sums had to fall six to eight orders of magnitude before the iterations were stopped. In addition, variable values at a location chosen in the region of steep gradients were monitored. They were chosen to be accurate to six most significant digits as well. The same kind of control was implemented for the integral features such as mass flux in an eddy and heat flux through a wall.

* This kind of error analysis was inspired by Ferziger.[13]

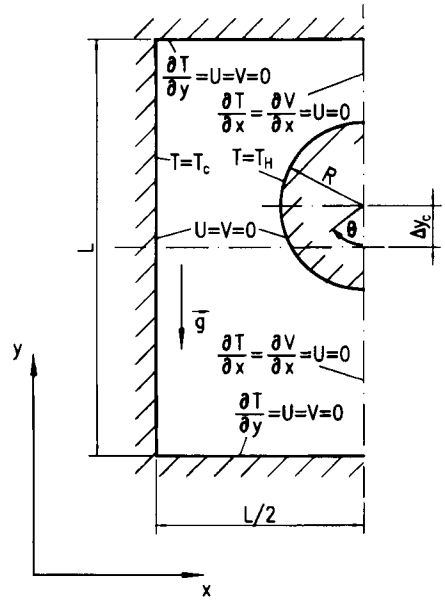

Figure 3. Geometry and boundary conditions for test case C4

The first type of error depends on the discretization scheme and the grid used. The order of the truncation error is often falsely interpreted as a measure of accuracy (one often finds statements in the literature like '. . . second-order accurate'). In fact, the order only states at which rate the error is reduced when the grid is refined, but it gives no information about the magnitude of the errors on a given grid. The truncation error, which acts as the source of the discretization error, depends on the grid spacing, higher-order derivatives of the dependent variable and—on non-orthogonal grids—on the angle between grid lines. As the grid is refined, the angle between grid lines and the variable derivatives at a given point tend to be constants; since they always appear as multipliers of the grid spacing, the truncation error—and therefore the discretization error—changes proportionally to the grid spacing to power n ($n=2$ for second-order schemes).[14]

By systematically refining the grid (doubling the number of CVs in each direction), it is possible to quantify the discretization error by evaluating the differences in solutions on consecutive grids.[3] The multigrid procedure used here provides solutions on a sequence of grids, e.g. from 10×10 to 320×320 CV (six grids), thus facilitating the error analysis. In the case of only first-order convergence, the discretization error on the finer grid would be of the order of the difference between the solutions on that and on the next coarser grid. For second-order schemes, the error is three times lower. In all the cases presented here the convergence is approximately of second order. Solutions from the finest grid will be presented and the difference to the next coarser grid solution will be given as a measure of the discretization error. The 'grid-independent' values can be obtained by means of Richardson extrapolation (adding one-third of the difference to the solution on the finer grid[3]).

3.1. Test case C1

Non-uniform grids, symmetrically expanding towards the centreline from all walls, were employed. The coarsest grid had 10×10 CV, the size of the smallest grid spacing near the wall

being $L/20$. By systematically refining this grid, the expansion ratio reduces as a square-root function, from 1·3524 on the coarsest grid to 1·0096 on the finest grid of 320×320 CV. However, the smallest Δx on this grid was $L/757$. Under-relaxation factors of 0·7–0·8 for velocities and 0·3–0·4 for pressure were used (lower values were used for $Re = 1000$). The computing times required to obtain solutions on all grids up to 160×160 CV at $Re = 1000$ were (253 iterations on the finest grid): 13 151 s on the SUN SPARCstation 1, 2753 s on the CYBER 995E and 633 s on CRAY YMP (no vectorization). The convergence criterion was, as earlier stated, the reduction of residual sums by seven orders of magnitude. For $Re = 100$, 70% less computing effort was required (91 iterations on the finest grid).

Figure 4 shows the streamlines for (a) $Re = 100$ and (b) $Re = 1000$. The difference in the solution for the two Reynolds numbers is substantial. For $Re = 100$, the main vortex fills almost the whole cavity. The first counterrotating vortex lies deep in the corner and is three orders of magnitude weaker. For $Re = 1000$, the primary vortex fills only about a third of the cavity. The largest vortex

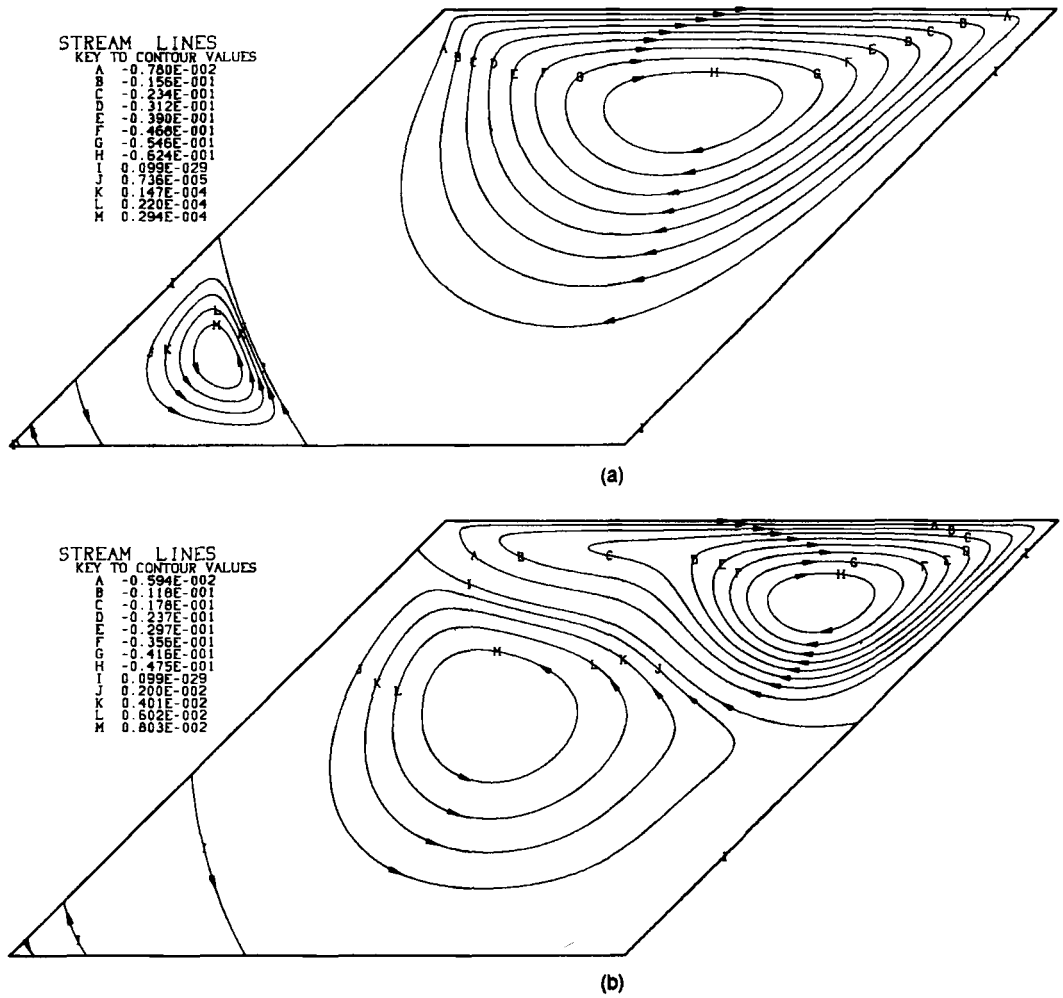

Figure 4. Predicted streamlines for test case C1, 320×320 CV grid: (a) $Re = 100$; (b) $Re = 1000$

is the second one, whose strength is only a factor of five lower than that of the primary vortex. The subsequent corner vortices are, as expected, about three orders of magnitude weaker. Their size can be accurately determined only if the results are accurate to more than five digits.

The stream function values indicate the mass flux inside the vortex. The maximum or minimum value in one vortex centre defines the total mass flow across any line connecting the vortex centre with the vortex boundary (zero streamline, cavity wall). For the two strongest vortices, these values, denoted as ψ_{min} (first vortex) and ψ_{max} (second vortex), were evaluated on all grids. Figures 5 and 6 show the convergence of ψ_{min} and ψ_{max} towards the grid-independent values as the grid is

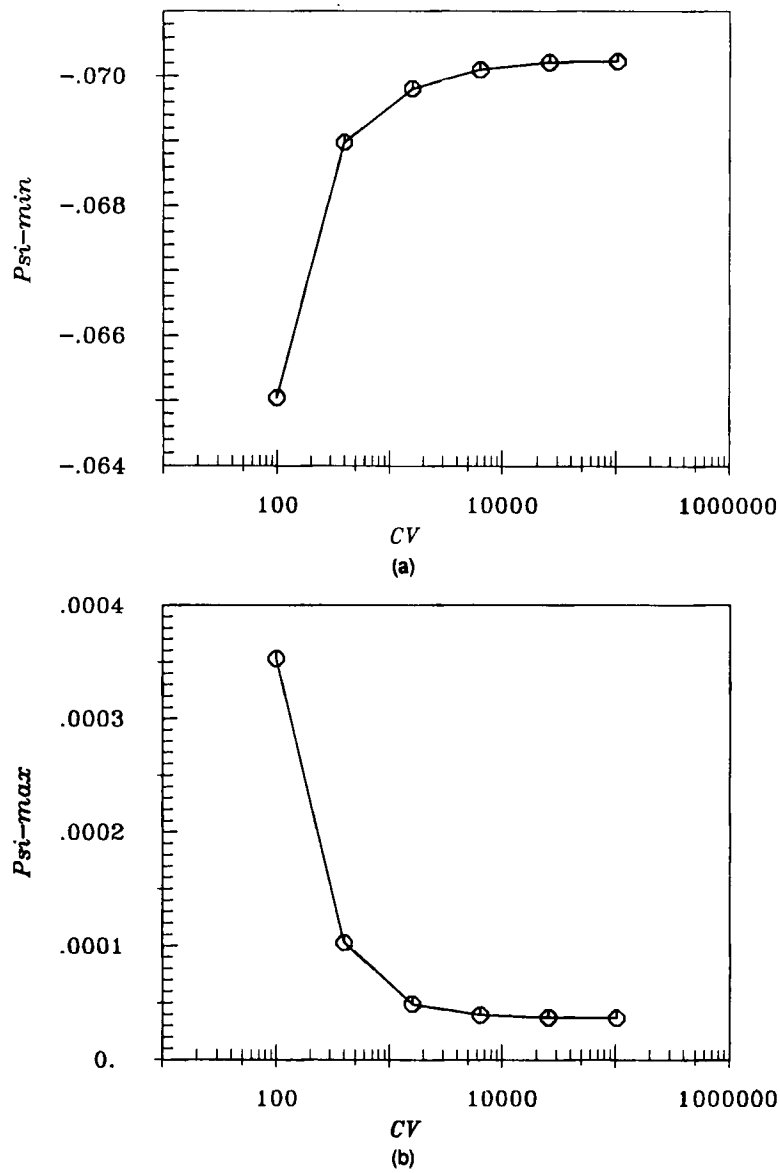

Figure 5. Variation of (a) minimum and (b) maximum stream function values in case C1, $Re = 100$, as a function of grid fineness

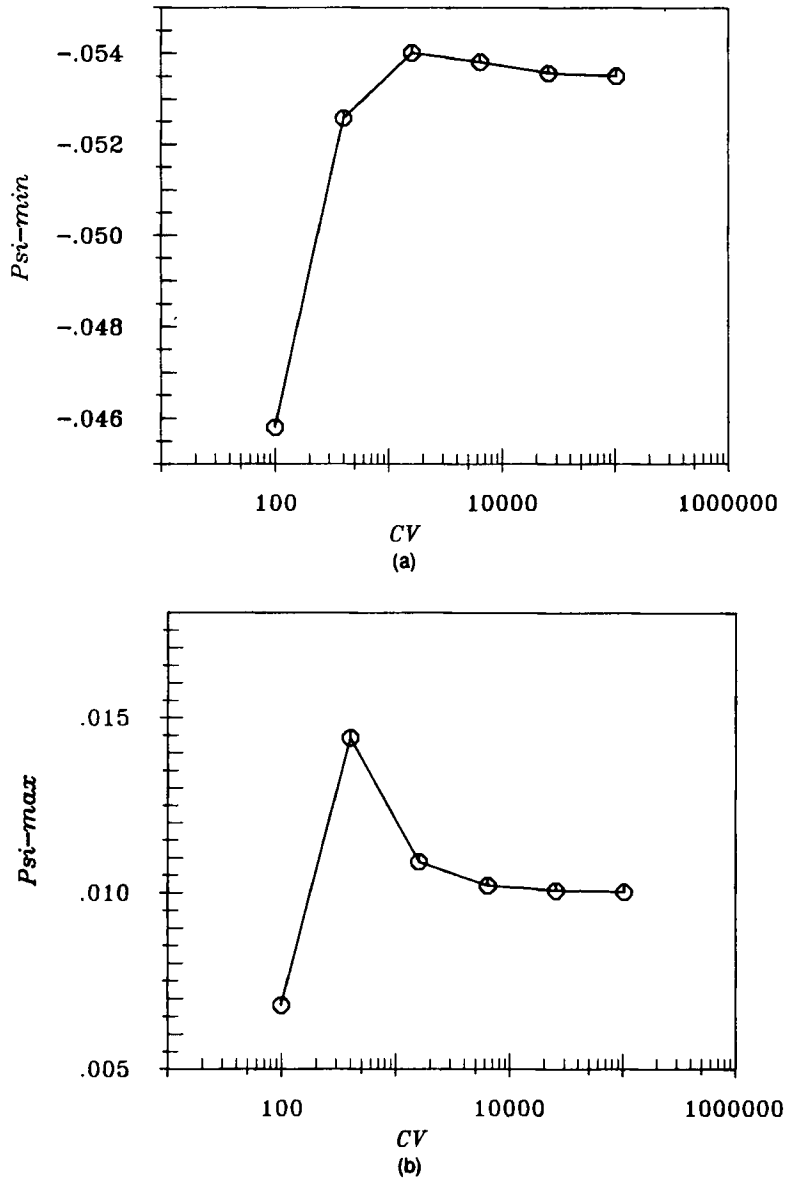

Figure 6. Variation of (a) minimum and (b) maximum stream function values in case C1, $Re = 1000$, as a function of grid fineness

refined for $Re = 100$ and $Re = 1000$, respectively. It is very interesting to note that in the case for $Re = 100$, monotonic convergence from the first grid onwards is observed for both ψ_{min} and ψ_{max}. However, for $Re = 1000$, ψ_{min} has a maximum on the third grid (40×40 CV) and ψ_{max} on the second grid (20×20 CV). If one had only solutions up to the grid with 40×40 CV, it would have been impossible to make an accurate estimate of the final value. However, the difference between the values obtained on the two consecutive grids is always decreasing, although not at a constant rate (second-order approximations used for both diffusive and convective fluxes). Thus, the

difference between the values obtained on the two last grids (160×160 and 320×320 CV) is a good measure of the accuracy of the final solution. Table I presents the ψ_{min} and ψ_{max} values calculated on the finest grid, together with the vortex centre co-ordinates and the error measure, ε, defined as:

$$\varepsilon = \left| \frac{\psi_{320} - \psi_{160}}{\psi_{320}} \right| \cdot 100. \tag{1}$$

The latter indicates the difference in the values obtained on 320×320 and 160×160 CV grids as a percentage of the finer-grid solution. Note that the second vortex is always weaker (especially for $Re = 100$), so that higher relative errors result.

Convergence of the solution is also illustrated in Figure 7, which shows for $Re = 1000$ the profiles of U- and V-velocity components along the centrelines indicated in Figure 1. Strong grid dependence is observed up to grid 4 (80×80 CV). The difference between the profiles obtained on the two finest grids is hardly visible. It is interesting that the V-profiles obtained on the two coarsest grids are even qualitatively different from the final solution. On the other hand, the difference between the profiles obtained from grid 3 to grid 6 is very small. These results indicate that in complex flow problems, the convergence of the solution method cannot be judged by monitoring one quantity change, especially not by monitoring a variable value at a single point. (There are points, e.g. at $x = 0{\cdot}3$ on the V-profile in Figure 7(b), where the profiles on all but the coarsest grid intersect; at this point, one would see large changes from grid 1 ($+0{\cdot}06$) to grid 2 ($-0{\cdot}04$) and no change thereafter which could lead to wrong conclusions.) The velocity profiles predicted on the finest grid are presented in tabulated form in Tables II (for $Re = 100$) and III (for $Re = 1000$). Only 15 points significant for the accurate reproduction of profile shape are given. The last two entries represent extremes in the profile. Note that the co-ordinate y^* for U and x^* for V is the normalized distance along the centreline and not the actual x- or y-co-ordinate.

3.2. Test case C2

In this case, the same type of grid as in case C1 was used. However, the angle between the grid lines was lower, namely 30°. The results of the calculations are similar to those obtained for case C1. The purpose of this test is to demonstrate the ability of the solution method to handle extreme

Table I. Minimum and maximum stream function values in vortex centres and their position, as predicted on the 320×320 CV grid for cases C1 and C2

	$\beta = 45°$		$\beta = 30°$	
Re	100	1000	100	1000
ψ_{min}	$-7{\cdot}0226 \times 10^{-2}$	$-5{\cdot}3507 \times 10^{-2}$	$-5{\cdot}3135 \times 10^{-2}$	$-3{\cdot}8563 \times 10^{-2}$
x	$1{\cdot}1100 \times 10^{-0}$	$1{\cdot}3130 \times 10^{-0}$	$1{\cdot}1664 \times 10^{-0}$	$1{\cdot}4583 \times 10^{-0}$
y	$5{\cdot}4638 \times 10^{-1}$	$5{\cdot}7404 \times 10^{-1}$	$3{\cdot}7898 \times 10^{-1}$	$4{\cdot}1086 \times 10^{-1}$
ε	0·0219405	0·1068854	0·0332841	0·0538782
ψ_{max}	$3{\cdot}6831 \times 10^{-5}$	$1{\cdot}0039 \times 10^{-2}$	$5{\cdot}6058 \times 10^{-5}$	$4{\cdot}1494 \times 10^{-3}$
x	$3{\cdot}3867 \times 10^{-1}$	$7{\cdot}7663 \times 10^{-1}$	$5{\cdot}2692 \times 10^{-1}$	$9{\cdot}0386 \times 10^{-1}$
y	$1{\cdot}4308 \times 10^{-1}$	$3{\cdot}9851 \times 10^{-1}$	$1{\cdot}4334 \times 10^{-1}$	$2{\cdot}5501 \times 10^{-1}$
ε	1·3554620	0·3313280	5·0257323	0·8776961

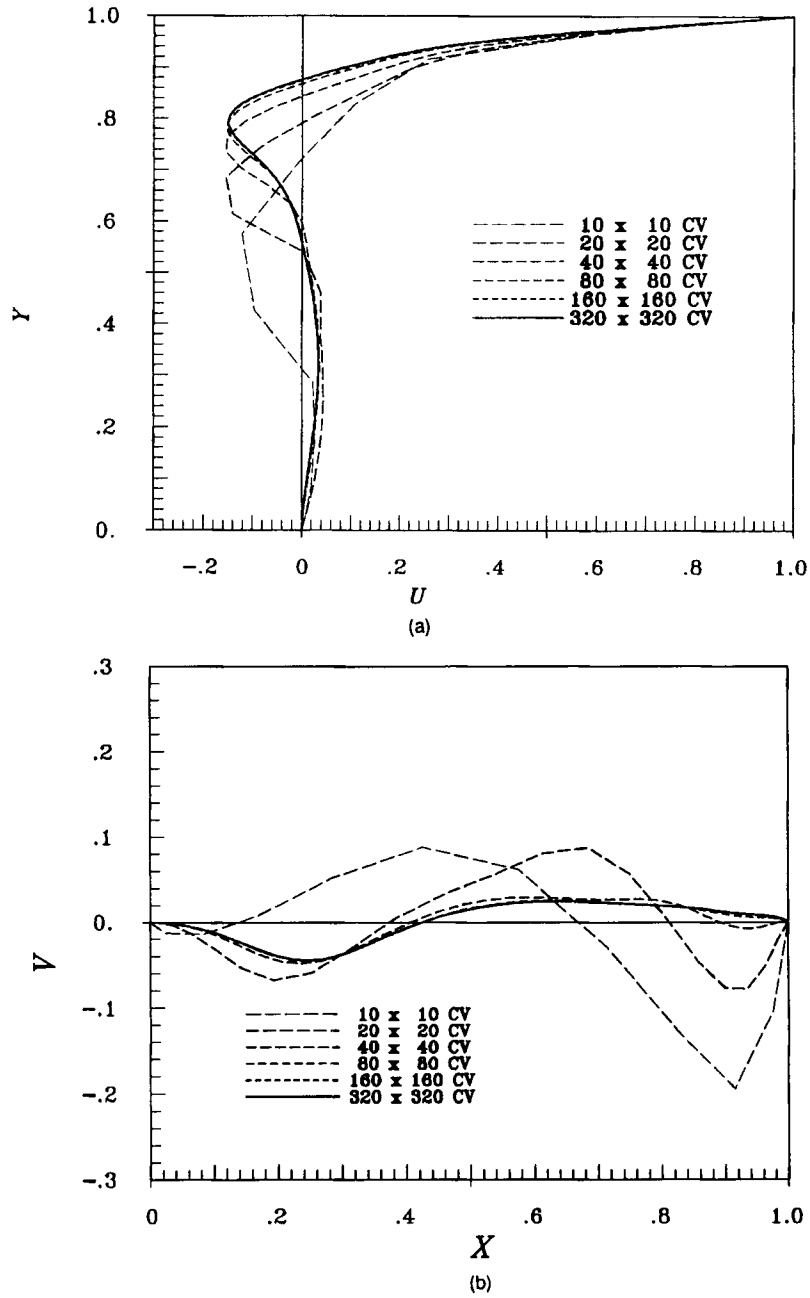

Figure 7. Variation of the centreline velocity profiles in case C1, $Re = 1000$, as a function of grid fineness: (a) U-component; (b) V-component

grid non-orthogonality. The number of iterations required to reach a solution of the same accuracy at the same Reynolds number was about the same in both cases C1 and C2.

Figure 8 presents the streamlines for (a) $Re = 100$ and (b) $Re = 1000$. They are similar to those of case C1 (cf. Figure 4). However, the number of corner vortices has increased (due to the smaller

Table II. Selected values of the centreline velocity profiles for case C1, $Re = 100$

$\beta = 45°$, $Re = 100$			
U	y^*	V	x^*
$-8{\cdot}0551 \times 10^{-3}$	$1{\cdot}1867 \times 10^{-1}$	$2{\cdot}1657 \times 10^{-3}$	$4{\cdot}9090 \times 10^{-2}$
$-2{\cdot}6196 \times 10^{-2}$	$2{\cdot}1817 \times 10^{-1}$	$1{\cdot}3305 \times 10^{-2}$	$1{\cdot}1867 \times 10^{-1}$
$-4{\cdot}3193 \times 10^{-2}$	$2{\cdot}8067 \times 10^{-1}$	$7{\cdot}6484 \times 10^{-2}$	$3{\cdot}0089 \times 10^{-1}$
$-6{\cdot}8882 \times 10^{-2}$	$3{\cdot}5234 \times 10^{-1}$	$9{\cdot}4120 \times 10^{-2}$	$3{\cdot}7109 \times 10^{-1}$
$-1{\cdot}5506 \times 10^{-1}$	$5{\cdot}3710 \times 10^{-1}$	$9{\cdot}5630 \times 10^{-2}$	$4{\cdot}5050 \times 10^{-1}$
$-1{\cdot}6634 \times 10^{-1}$	$5{\cdot}7535 \times 10^{-1}$	$8{\cdot}2656 \times 10^{-2}$	$5{\cdot}0752 \times 10^{-1}$
$-1{\cdot}6872 \times 10^{-1}$	$6{\cdot}1198 \times 10^{-1}$	$4{\cdot}6757 \times 10^{-2}$	$5{\cdot}8459 \times 10^{-1}$
$-1{\cdot}5730 \times 10^{-1}$	$6{\cdot}5230 \times 10^{-1}$	$-3{\cdot}8092 \times 10^{-3}$	$6{\cdot}5688 \times 10^{-1}$
$-1{\cdot}3105 \times 10^{-1}$	$6{\cdot}8792 \times 10^{-1}$	$-1{\cdot}1270 \times 10^{-1}$	$7{\cdot}8552 \times 10^{-1}$
$-8{\cdot}9766 \times 10^{-2}$	$7{\cdot}2125 \times 10^{-1}$	$-1{\cdot}4721 \times 10^{-1}$	$8{\cdot}3908 \times 10^{-1}$
$-3{\cdot}4731 \times 10^{-2}$	$7{\cdot}5234 \times 10^{-1}$	$-1{\cdot}5539 \times 10^{-1}$	$8{\cdot}6249 \times 10^{-1}$
$3{\cdot}3532 \times 10^{-2}$	$7{\cdot}8185 \times 10^{-1}$	$-1{\cdot}5682 \times 10^{-1}$	$8{\cdot}8885 \times 10^{-1}$
$2{\cdot}0103 \times 10^{-1}$	$8{\cdot}3600 \times 10^{-1}$	$-1{\cdot}4635 \times 10^{-1}$	$9{\cdot}1682 \times 10^{-1}$
$3{\cdot}8137 \times 10^{-1}$	$8{\cdot}8128 \times 10^{-1}$	$-1{\cdot}1141 \times 10^{-1}$	$9{\cdot}5078 \times 10^{-1}$
$5{\cdot}5574 \times 10^{-1}$	$9{\cdot}1906 \times 10^{-1}$	$-6{\cdot}5443 \times 10^{-2}$	$9{\cdot}7578 \times 10^{-1}$
		$9{\cdot}77007 \times 10^{-2}$	$4{\cdot}18010 \times 10^{-1}$
$-1{\cdot}69100 \times 10^{-1}$	$6{\cdot}02904 \times 10^{-1}$	$-1{\cdot}57402 \times 10^{-1}$	$8{\cdot}78699 \times 10^{-1}$

Table III. Selected values of the centreline velocity profiles for case C1, $Re = 1000$

$\beta = 45°$, $Re = 1000$			
U	y^*	V	x^*
$2{\cdot}6907 \times 10^{-2}$	$2{\cdot}1455 \times 10^{-1}$	$-3{\cdot}3552 \times 10^{-3}$	$4{\cdot}9090 \times 10^{-2}$
$3{\cdot}4145 \times 10^{-2}$	$3{\cdot}0917 \times 10^{-1}$	$-1{\cdot}3235 \times 10^{-2}$	$1{\cdot}0355 \times 10^{-1}$
$2{\cdot}8952 \times 10^{-2}$	$4{\cdot}0864 \times 10^{-1}$	$-3{\cdot}9715 \times 10^{-2}$	$2{\cdot}0064 \times 10^{-1}$
$-8{\cdot}7552 \times 10^{-3}$	$5{\cdot}9377 \times 10^{-1}$	$-4{\cdot}3934 \times 10^{-2}$	$2{\cdot}2950 \times 10^{-1}$
$-2{\cdot}1473 \times 10^{-2}$	$6{\cdot}2988 \times 10^{-1}$	$-4{\cdot}4009 \times 10^{-2}$	$2{\cdot}6066 \times 10^{-1}$
$-4{\cdot}0688 \times 10^{-2}$	$6{\cdot}6593 \times 10^{-1}$	$-3{\cdot}9277 \times 10^{-2}$	$2{\cdot}9272 \times 10^{-1}$
$-6{\cdot}8730 \times 10^{-2}$	$7{\cdot}0070 \times 10^{-1}$	$-3{\cdot}0630 \times 10^{-2}$	$3{\cdot}2594 \times 10^{-1}$
$-1{\cdot}3455 \times 10^{-1}$	$7{\cdot}6352 \times 10^{-1}$	$-8{\cdot}9834 \times 10^{-3}$	$3{\cdot}9456 \times 10^{-1}$
$-1{\cdot}4954 \times 10^{-1}$	$7{\cdot}9275 \times 10^{-1}$	$7{\cdot}9812 \times 10^{-3}$	$4{\cdot}5984 \times 10^{-1}$
$-1{\cdot}4412 \times 10^{-1}$	$8{\cdot}1013 \times 10^{-1}$	$1{\cdot}4868 \times 10^{-2}$	$4{\cdot}9756 \times 10^{-1}$
$-1{\cdot}1001 \times 10^{-1}$	$8{\cdot}3600 \times 10^{-1}$	$2{\cdot}2300 \times 10^{-2}$	$5{\cdot}6594 \times 10^{-1}$
$-5{\cdot}1863 \times 10^{-2}$	$8{\cdot}5968 \times 10^{-1}$	$2{\cdot}4068 \times 10^{-2}$	$6{\cdot}0290 \times 10^{-1}$
$1{\cdot}6822 \times 10^{-1}$	$9{\cdot}1906 \times 10^{-1}$	$2{\cdot}4119 \times 10^{-2}$	$6{\cdot}7483 \times 10^{-1}$
$2{\cdot}5888 \times 10^{-1}$	$9{\cdot}3598 \times 10^{-1}$	$1{\cdot}7954 \times 10^{-2}$	$8{\cdot}2974 \times 10^{-1}$
$4{\cdot}4780 \times 10^{-1}$	$9{\cdot}5859 \times 10^{-1}$	$4{\cdot}7042 \times 10^{-3}$	$9{\cdot}8672 \times 10^{-1}$
$3{\cdot}4331 \times 10^{-2}$	$3{\cdot}25940 \times 10^{-1}$	$2{\cdot}4576 \times 10^{-2}$	$6{\cdot}3879 \times 10^{-1}$
$-1{\cdot}4954 \times 10^{-1}$	$7{\cdot}92748 \times 10^{-1}$	$-4{\cdot}4582 \times 10^{-2}$	$2{\cdot}4492 \times 10^{-1}$

angle β). The mass flow rates in the two main vortices, corresponding to the maximum or minimum stream function value inside the vortex, are given in Table I together with those of case C1. The primary vortex, driven by the lid movement, is weaker in the C2 case due to the smaller volume of the cavity. Actually, the $\psi_{\min}$ values for the two cases for both Reynolds numbers relate

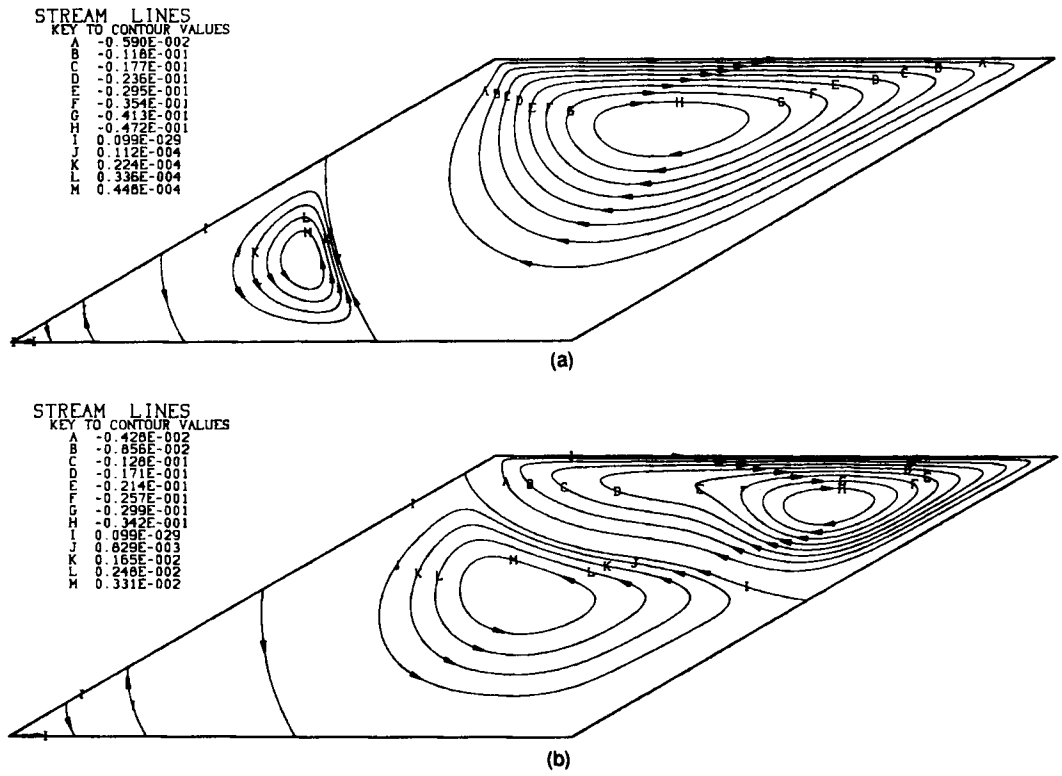

Figure 8. Predicted streamlines for test case C2, 320 x 320 CV grid: (a) $Re = 100$; (b) $Re = 1000$

to each other approximately like cavity areas. The second vortex is also stronger in the C1 case, except at low Reynolds numbers when it is confined to the corner and hence stronger at lower β angles. Convergence of the ψ_{min} and ψ_{max} values in case C2 is qualitatively the same as in case C1 (cf. Figures 5 and 6). The difference between the values calculated on the two last grids (cf. equation (1)) is given in Table I. The co-ordinates of the vortex centres are also given in Table I.

The centreline velocity profiles, as predicted on all six grids, are presented in Figure 9 for $Re = 1000$. They indicate that an accurate profile description is obtained from the 80 x 80 CV grid onwards, the last two grids being indistinguishable. The fact that the difference between the profiles obtained on 80 x 80 and 160 x 160 CV grids is much lower than the difference between those obtained on 40 x 40 and 80 x 80 CV grids indicates that the order of convergence corresponds to the order of the flux approximation (second-order central differences). However, analysing the variable values at a given point could also be misleading here, since there are points on the profiles at which almost all of the grids yield identical values. The centreline profiles of the U- and V-velocity components, obtained on the 320 x 320 CV grid, are presented in tabulated form in Tables IV ($Re = 100$) and V ($Re = 1000$). Only 15 points significant for the description of the profile are given. The last two entries represent maximums or minimums on the profile. The co-ordinates x^* and y^* represent the relative distance between the cavity walls.

3.3. Test case C3

The geometry of this test case is identical to that of case C1. However, the flow is driven by buoyancy and, in addition to the Navier–Stokes equations, an equation for temperature has to be

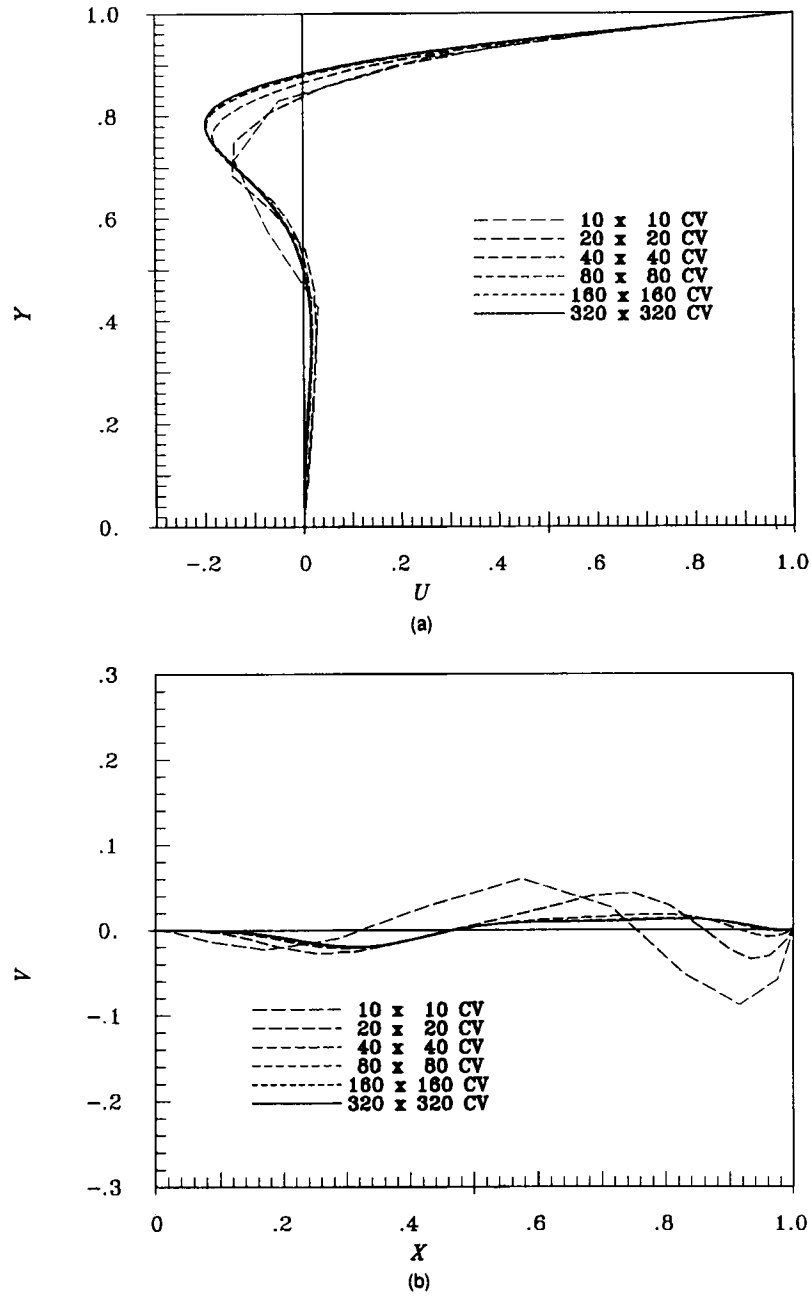

Figure 9. Variation of the centreline velocity profiles in case C2, $Re = 1000$, as a function of grid fineness: (a) U-component; (b) V-component

solved. The temperature is coupled with the velocity field through the convection terms, and the velocity field is coupled with the temperature through the buoyancy term which acts as a source of momentum: for example, in this particular case, the V-equation contains a source term:

$$S_V^b = \rho_0 g \beta (T - T_0) \delta V,$$

Table IV. Selected values of the centreline velocity profiles for case C2, $Re = 100$

$\beta = 30°$, $Re = 100$			
U	y^*	V	x^*
$-5{\cdot}3649 \times 10^{-3}$	$2{\cdot}0406 \times 10^{-1}$	$3{\cdot}9397 \times 10^{-3}$	$1{\cdot}6518 \times 10^{-1}$
$-1{\cdot}4682 \times 10^{-2}$	$2{\cdot}6463 \times 10^{-1}$	$2{\cdot}1914 \times 10^{-2}$	$2{\cdot}4882 \times 10^{-1}$
$-3{\cdot}2040 \times 10^{-2}$	$3{\cdot}3022 \times 10^{-1}$	$9{\cdot}3419 \times 10^{-2}$	$4{\cdot}1333 \times 10^{-1}$
$-7{\cdot}1895 \times 10^{-2}$	$4{\cdot}1801 \times 10^{-1}$	$1{\cdot}0104 \times 10^{-1}$	$4{\cdot}5050 \times 10^{-1}$
$-1{\cdot}4988 \times 10^{-1}$	$5{\cdot}3222 \times 10^{-1}$	$9{\cdot}8228 \times 10^{-2}$	$4{\cdot}9756 \times 10^{-1}$
$-1{\cdot}7111 \times 10^{-1}$	$5{\cdot}7066 \times 10^{-1}$	$8{\cdot}4957 \times 10^{-2}$	$5{\cdot}3710 \times 10^{-1}$
$-1{\cdot}7947 \times 10^{-1}$	$6{\cdot}0745 \times 10^{-1}$	$6{\cdot}4102 \times 10^{-2}$	$5{\cdot}7535 \times 10^{-1}$
$-1{\cdot}7619 \times 10^{-1}$	$6{\cdot}2988 \times 10^{-1}$	$3{\cdot}8595 \times 10^{-2}$	$6{\cdot}1198 \times 10^{-1}$
$-1{\cdot}6196 \times 10^{-1}$	$6{\cdot}5688 \times 10^{-1}$	$-7{\cdot}3152 \times 10^{-2}$	$7{\cdot}4856 \times 10^{-1}$
$-1{\cdot}4573 \times 10^{-1}$	$6{\cdot}7483 \times 10^{-1}$	$-1{\cdot}1133 \times 10^{-1}$	$8{\cdot}0673 \times 10^{-1}$
$-9{\cdot}9249 \times 10^{-2}$	$7{\cdot}0905 \times 10^{-1}$	$-1{\cdot}2854 \times 10^{-1}$	$8{\cdot}5683 \times 10^{-1}$
$3{\cdot}3969 \times 10^{-2}$	$7{\cdot}7087 \times 10^{-1}$	$-1{\cdot}2915 \times 10^{-1}$	$8{\cdot}7870 \times 10^{-1}$
$1{\cdot}9969 \times 10^{-1}$	$8{\cdot}2656 \times 10^{-1}$	$-1{\cdot}1649 \times 10^{-1}$	$9{\cdot}1682 \times 10^{-1}$
$5{\cdot}2529 \times 10^{-1}$	$9{\cdot}1237 \times 10^{-1}$	$-8{\cdot}6419 \times 10^{-2}$	$9{\cdot}5078 \times 10^{-1}$
$7{\cdot}7295 \times 10^{-1}$	$9{\cdot}6328 \times 10^{-1}$	$-4{\cdot}9836 \times 10^{-2}$	$9{\cdot}7578 \times 10^{-1}$
		$1{\cdot}0172 \times 10^{-1}$	$4{\cdot}6449 \times 10^{-1}$
$-1{\cdot}7947 \times 10^{-1}$	$6{\cdot}0745 \times 10^{-1}$	$-1{\cdot}2951 \times 10^{-1}$	$8{\cdot}7074 \times 10^{-1}$

Table V. Selected values of the centreline velocity profiles for case C2, $Re = 1000$

$\beta = 30°$, $Re = 1000$			
U	y^*	V	x^*
$2{\cdot}2062 \times 10^{-3}$	$1{\cdot}1867 \times 10^{-1}$	$-6{\cdot}9812 \times 10^{-4}$	$8{\cdot}0811 \times 10^{-2}$
$1{\cdot}6317 \times 10^{-2}$	$3{\cdot}7578 \times 10^{-1}$	$-5{\cdot}3627 \times 10^{-3}$	$1{\cdot}6518 \times 10^{-1}$
$1{\cdot}0790 \times 10^{-2}$	$4{\cdot}5050 \times 10^{-1}$	$-1{\cdot}6489 \times 10^{-2}$	$2{\cdot}6066 \times 10^{-1}$
$-8{\cdot}3579 \times 10^{-3}$	$5{\cdot}2733 \times 10^{-1}$	$-1{\cdot}9262 \times 10^{-2}$	29272×10^{-1}
$-3{\cdot}5472 \times 10^{-2}$	$5{\cdot}8459 \times 10^{-1}$	$-1{\cdot}9873 \times 10^{-2}$	$3{\cdot}2594 \times 10^{-1}$
$-6{\cdot}4159 \times 10^{-2}$	$6{\cdot}2541 \times 10^{-1}$	$-1{\cdot}9073 \times 10^{-2}$	$3{\cdot}4326 \times 10^{-1}$
$-1{\cdot}6661 \times 10^{-1}$	$7{\cdot}2919 \times 10^{-1}$	$-1{\cdot}4969 \times 10^{-2}$	$3{\cdot}8046 \times 10^{-1}$
$-1{\cdot}9062 \times 10^{-1}$	$7{\cdot}5981 \times 10^{-1}$	$-1{\cdot}6780 \times 10^{-3}$	$4{\cdot}5984 \times 10^{-1}$
$-1{\cdot}9730 \times 10^{-1}$	$7{\cdot}8916 \times 10^{-1}$	$3{\cdot}8694 \times 10^{-3}$	$5{\cdot}0251 \times 10^{-1}$
$-1{\cdot}8630 \times 10^{-1}$	$8{\cdot}1013 \times 10^{-1}$	$8{\cdot}1783 \times 10^{-3}$	$5{\cdot}7066 \times 10^{-1}$
$-1{\cdot}4854 \times 10^{-1}$	$8{\cdot}3600 \times 10^{-1}$	$1{\cdot}2103 \times 10^{-2}$	$8{\cdot}2009 \times 10^{-1}$
$-8{\cdot}6502 \times 10^{-2}$	$8{\cdot}5968 \times 10^{-1}$	$1{\cdot}1023 \times 10^{-2}$	$8{\cdot}7074 \times 10^{-1}$
$-4{\cdot}2563 \times 10^{-3}$	$8{\cdot}8128 \times 10^{-1}$	$8{\cdot}5607 \times 10^{-3}$	$9{\cdot}0093 \times 10^{-1}$
$2{\cdot}1071 \times 10^{-1}$	$9{\cdot}1906 \times 10^{-1}$	$4{\cdot}2321 \times 10^{-4}$	$9{\cdot}6328 \times 10^{-1}$
$4{\cdot}6542 \times 10^{-1}$	$9{\cdot}4916 \times 10^{-1}$	$-8{\cdot}4611 \times 10^{-4}$	$9{\cdot}8828 \times 10^{-1}$
$1{\cdot}6344 \times 10^{-2}$	$3{\cdot}7109 \times 10^{-1}$	$1{\cdot}2123 \times 10^{-2}$	$8{\cdot}2656 \times 10^{-1}$
$-1{\cdot}9772 \times 10^{-1}$	$7{\cdot}8185 \times 10^{-1}$	$-1{\cdot}9979 \times 10^{-2}$	$3{\cdot}1751 \times 10^{-1}$

where T_0 and ρ_0 are the reference temperature and the corresponding density, and T is the temperature at the centre of the control volume δV. There is neither inflow nor outflow, and the strength of the recirculating flow depends only on the Rayleigh and Prandtl numbers. The aim of this test case is to assess the accuracy and convergence properties of the solution in the presence of the above additional coupling on a grid with an angle of 45° between grid lines.

The under-relaxation factors used in all the calculations for C3 were: 0·5–0·6 for velocities, 0·2–0·3 for pressure and 0·7–0·8 for temperature (lower values for $Pr = 0{\cdot}1$). They were not optimized for minimum computing effort. At $Pr = 10$, about 60 fine-grid iterations were required for convergence. At $Pr = 0{\cdot}1$, the rate of convergence was about five times slower. Figure 10 shows the grids used in the calculations (a quarter of each of the first four grids). The coarsest grid had 14×12 CV in the x- and y-direction, respectively, non-uniformly distributed so that the highest resolution was achieved near the walls. The finest grid had 224×192 CV with the smallest δx and δy amounting to $L/467$ and $L/454$, respectively.

For reference purposes, the pure heat conduction problem was solved first. Figure 11 shows the isotherms of this case. In a square cavity, the temperature distribution would have been linear so that the isotherms would be straight vertical lines. In the present case, the temperature distribution is more complex, since the adiabatic horizontal walls form an angle β with the isothermal walls (the isotherms must be orthogonal to the adiabatic walls, except for the two isothermal walls which form the angle β; cf. Figure 11). It is interesting to note that the total heat flux through the isothermal walls, Q_C, is the same in a square cavity and in a cavity squeezed to $\beta = 45°$.

The predicted flow patterns for $Ra = 10^6$ and for the two Prandtl numbers studied, 0·1 and 10, are shown in Figure 12. It is obvious that the Prandtl number has a significant influence on the flow and heat transfer.

For $Pr = 10$, the flow is directed along the walls and it stays attached to them, forming a single roll. In the case of $Pr = 0{\cdot}1$, the main current in the recirculating region tends to separate from the horizontal walls (cf. Figure 12(a)). Another big difference is that for $Pr = 0{\cdot}1$, a large region of slowly moving fluid is formed in the central part of the cavity, including two free stagnation points and a counterrotating eddy in the centre. This complex streamline pattern is recognizable already on the coarsest grid. In the case of $Pr = 10$, one free stagnation point exists in the cavity centre, but there are no counterrotating eddies.

Figure 13 shows the isotherms for the two Prandtl numbers. Their difference reflects the difference in flow patterns seen in Figure 12. The effect of convection is obvious from the comparison of Figures 13 and 11. Temperature gradients are steep near the isothermal walls, and a large stably stratified central region with horizontal isotherms results at both Prandtl numbers as a consequence of the convection process.

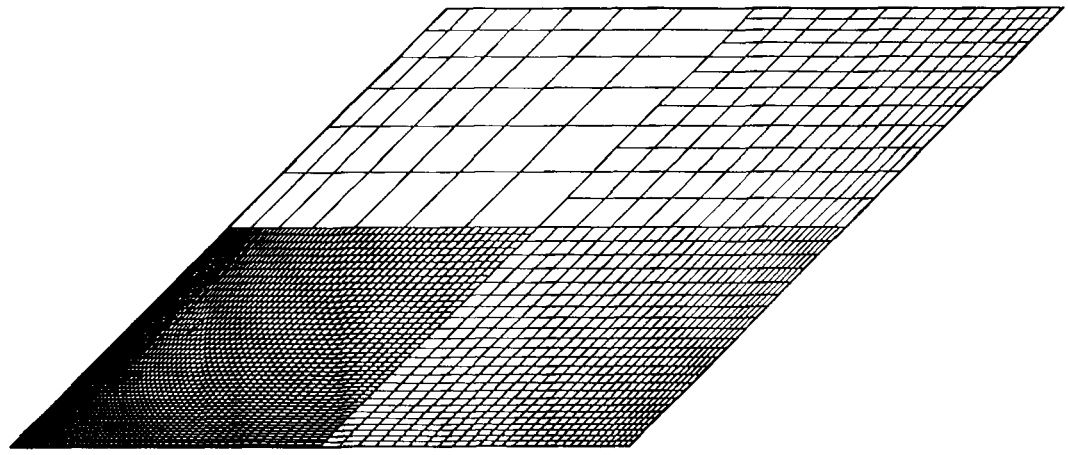

Figure 10. Segments of the first four grids used for case C3 (one-quarter of each)

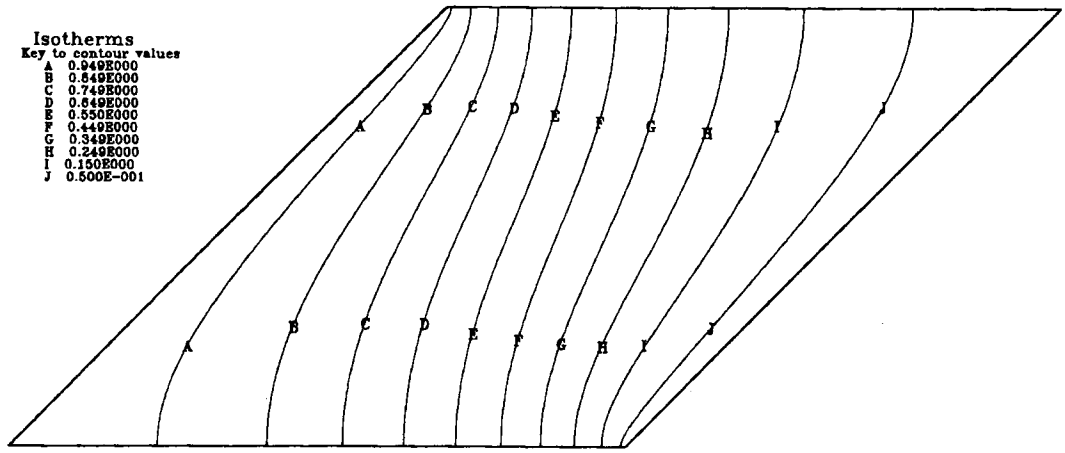

Figure 11. Isotherms of case C3 for pure conduction heat transfer

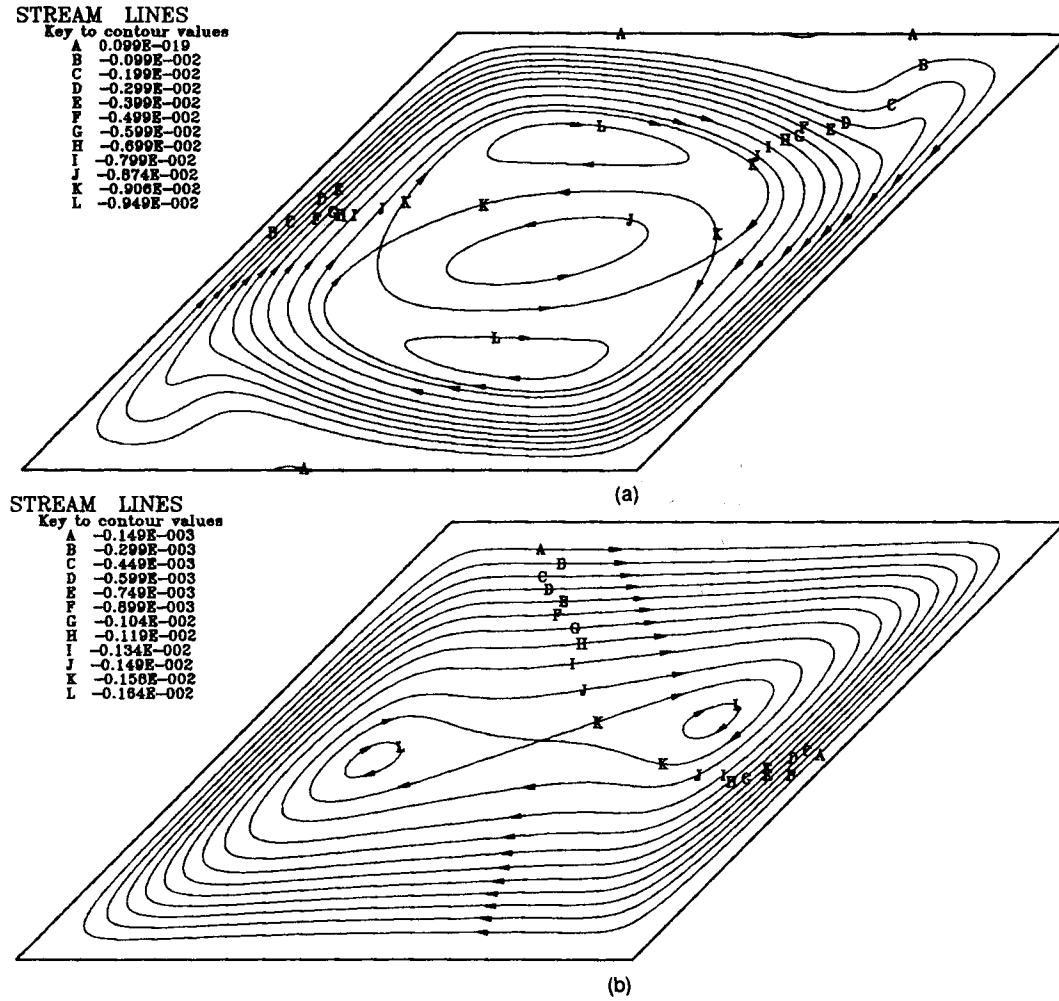

Figure 12. Predicted streamlines for case C3 on the 224 × 192 CV grid: (a) $Pr = 0{\cdot}1$; (b) $Pr = 10$

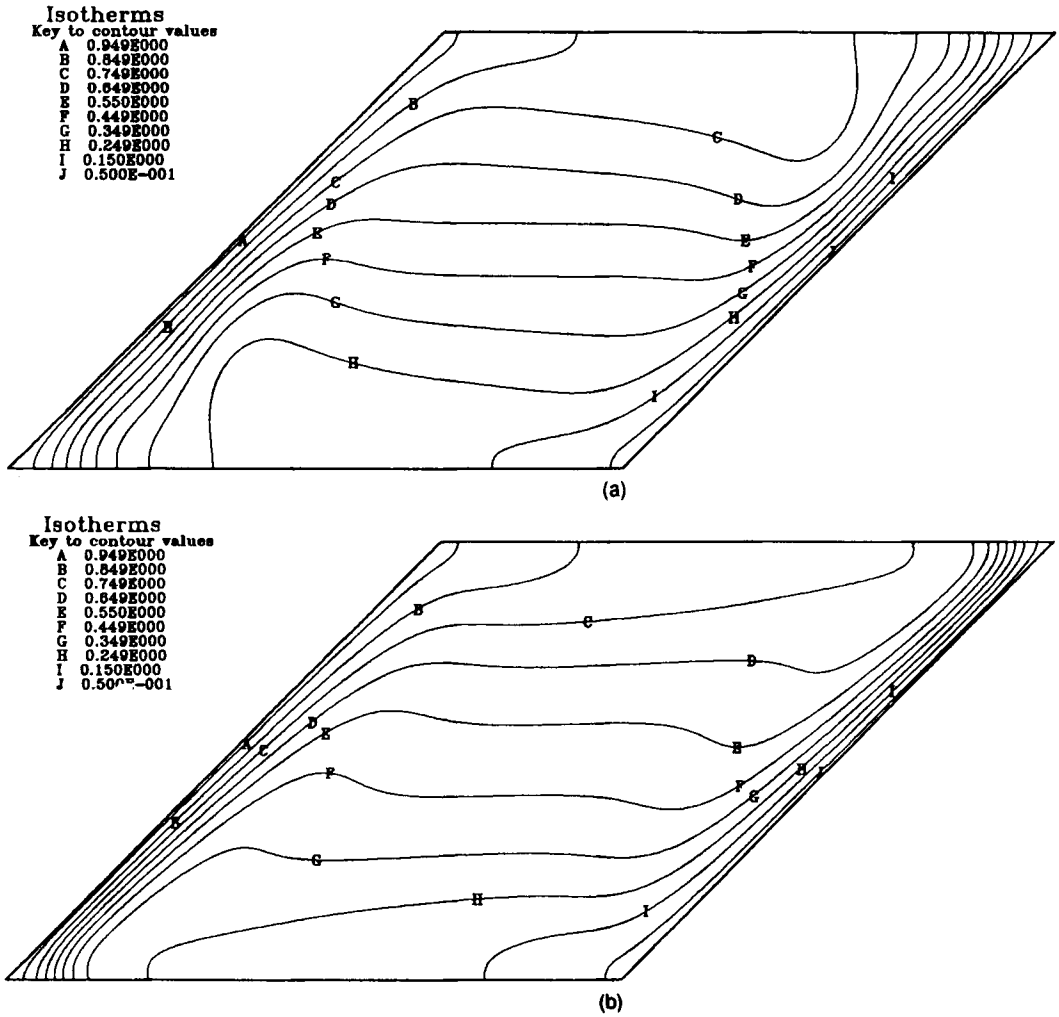

Figure 13. Predicted isotherms for case C3 on the 224 × 192 CV grid: (a) $Pr = 0{\cdot}1$; (b) $Pr = 10$

Heat fluxes through the two isothermal walls and through any cross-section between the two adiabatic walls must be identical. In our conservative solution method, this is automatically ensured on any grid to within the convergence accuracy, here to six most significant figures. The total heat flux through one wall was normalized by the conduction heat flux of the square cavity, defined as

$$Q_N = \frac{\mu C_p}{Pr} \frac{T_H - T_C}{L} \cdot L \cdot 1,$$

thus giving the average Nusselt number, $\overline{Nu}$. Note that here $Q_C = Q_N$.

Local heat fluxes per unit area, normalized with the normalization heat flux Q_N per unit area, represent the local Nusselt numbers. Table VI presents the values of the average and maximum Nusselt numbers, $\overline{Nu}$ and Nu_{max}, at the cold wall, the position of Nu_{max}, and the minimum and

TableVI. Characteristic Nusselt numbers and stream function values for cases C3 and C4 as predicted on the finest grid

	C3		C4	
Pr	0·1	10	0·1	10
$\overline{Nu}$	5·98493	7·58013	6·73036	7·38376
ε	0·0814	0·0516	0·022	0·088
$Nu_{y,\max}$	8·6778	12·471	14·558	19·949
y^*	0·45644	0·17028	0·87891	0·96484
$Nu_{\theta,\max}$	—	—	21·300	18·592
θ	—	—	20·186	0·000
Nu^C	1·0	1·0	2·31407	2·31407
$\psi_{\min}$	$-9{\cdot}68706\times10^{-3}$	$-1{\cdot}662127\times10^{-3}$	$-8{\cdot}78350\times10^{-5}$	—
x	0·78926	0·57276	0·46453	—
y	0·178134	0·319989	0·05430	—
ε	0·00016	0·0063	0·5	—
$\psi_{\max}$	$7{\cdot}705\times10^{-8}$	—	$1{\cdot}212974\times10^{-2}$	$1{\cdot}419586\times10^{-3}$
x	1·271738	—	0·27188	0·149187
y	0·702687	—	0·24593	0·668196
ε	200	—	0·104	0·063

maximum values of the stream function in the vortex centres with their position. Since the conductivity coefficient equals μ/Pr, the conduction heat transfer is an order of magnitude higher for $Pr=0{\cdot}1$ than for $Pr=10$. However, the Nusselt number is higher in the case of higher Prandtl numbers. Also shown is the difference between the $\overline{Nu}$-values at the two finest grids, ε, expressed as a percentage of $\overline{Nu}$, as well as the corresponding information for the stream function values (cf. equation (1)). The accuracy is better than 0·1% in all cases, except for the stream function values in extremely weak vortices. Note also that y^* represents the normalized co-ordinate along the wall.

Flow at $Pr=10$ was also predicted on uniform grids with the same number of control volumes. The number of iterations necessary to reach the convergence criterion was about 10% higher for the uniform than for the non-uniform grid (57 iterations on the finest grid; the sum of absolute residuals less than 10^{-9} for all variables; the initial absolute residual sums of the order of 10^{-2}). Figure 14 shows the convergence of (a) the average Nusselt number $\overline{Nu}$ and (b) the minimum value of the stream function $\psi_{\min}$ as the grid is refined for both uniform and non-uniform arrangements. The non-uniform grid solutions are obviously more accurate at the same number of control volumes, but in both cases a convergence towards the same grid-independent value results. The rate of convergence is approximately second-order for both grid types.

Table VII presents the variation of the local Nusselt number along the cold wall for $Pr=0{\cdot}1$ and 10, respectively, as calculated on the finest grid. Again, only 15 characteristic points are given, which are sufficient to describe the profile accurately. The four extra entries specify the extreme values on the profile (for $Pr=10$, there is only one maximum and one minimum, while for $Pr=0{\cdot}1$ there are two of each).

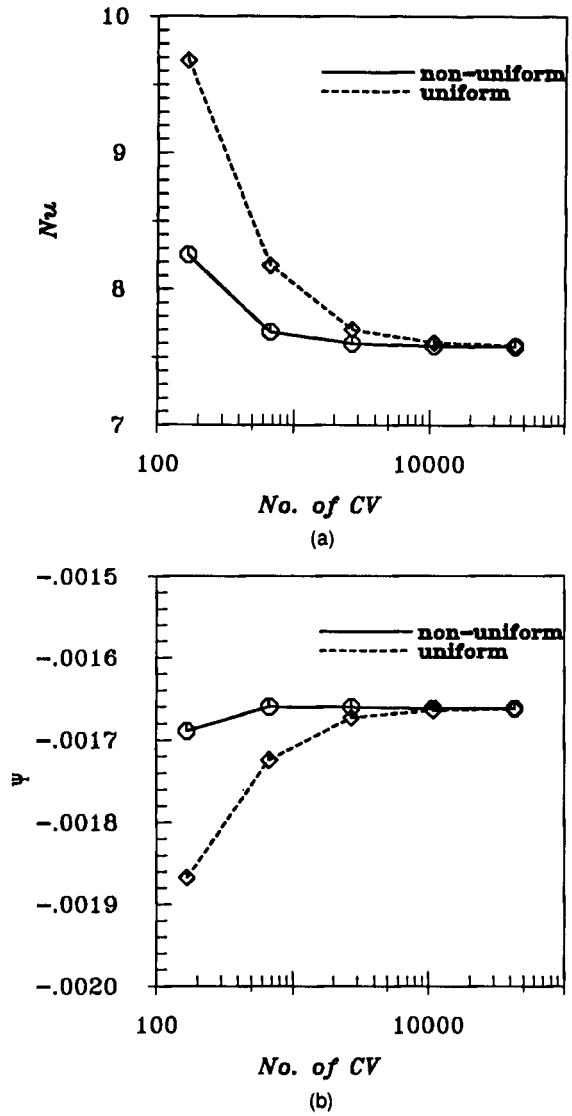

Figure 14. Convergence of (a) the average Nusselt number and (b) the minimum stream function value towards the grid-independent solution in case C3, $Pr = 10$, on uniform and non-uniform grids

3.4. Test case C4

This test case requires the use of a more complex, non-uniform and non-orthogonal grid (cf. Figure 15). Both the aspect and expansion ratios of the control volumes, as well as the inclination angle of grid lines, β, vary in a large range. This case simulates the complex geometries which are often encountered in practice. Figure 15 shows parts of the first four grids (one-quarter of each). The coarsest grid has 16×8 CV and the finest (fifth) grid has 256×128 CV. In all the calculations, the following under-relaxation parameters were used: 0·5 for velocities, 0·3 for pressure and 0·7 for temperature. About 200 fine-grid iterations were required to reach the convergence criterion

Table VII. Selected values of the profile of the local Nusselt number along the cold wall for case C3 as predicted on the 224 × 192 CV grid

$Pr = 0{\cdot}1$		$Pr = 10$	
Nu_y	y	Nu_y	y
$9{\cdot}8089 \times 10^{-2}$	$1{\cdot}4309 \times 10^{-3}$	$1{\cdot}9757 \times 10^{-1}$	$1{\cdot}4309 \times 10^{-3}$
$5{\cdot}8932 \times 10^{0}$	$1{\cdot}0000 \times 10^{-1}$	$8{\cdot}1249 \times 10^{0}$	$6{\cdot}5813 \times 10^{-2}$
$7{\cdot}3492 \times 10^{0}$	$1{\cdot}5148 \times 10^{-1}$	$1{\cdot}0674 \times 10^{1}$	$9{\cdot}6025 \times 10^{-2}$
$7{\cdot}5761 \times 10^{0}$	$1{\cdot}8001 \times 10^{-1}$	$1{\cdot}2051 \times 10^{1}$	$1{\cdot}2916 \times 10^{-1}$
$7{\cdot}5941 \times 10^{0}$	$1{\cdot}9504 \times 10^{-1}$	$1{\cdot}2428 \times 10^{1}$	$1{\cdot}5610 \times 10^{-1}$
$7{\cdot}4311 \times 10^{0}$	$2{\cdot}5481 \times 10^{-1}$	$1{\cdot}2471 \times 10^{1}$	$1{\cdot}7028 \times 10^{-1}$
$7{\cdot}4024 \times 10^{0}$	$2{\cdot}7850 \times 10^{-1}$	$1{\cdot}2445 \times 10^{1}$	$1{\cdot}8497 \times 10^{-1}$
$7{\cdot}5297 \times 10^{0}$	$3{\cdot}1617 \times 10^{-1}$	$1{\cdot}2083 \times 10^{1}$	$2{\cdot}3220 \times 10^{-1}$
$8{\cdot}6385 \times 10^{0}$	$4{\cdot}3316 \times 10^{-1}$	$1{\cdot}1208 \times 10^{1}$	$3{\cdot}0334 \times 10^{-1}$
$8{\cdot}6787 \times 10^{0}$	$4{\cdot}5644 \times 10^{-1}$	$8{\cdot}1111 \times 10^{0}$	$5{\cdot}2954 \times 10^{-1}$
$8{\cdot}2469 \times 10^{0}$	$5{\cdot}2122 \times 10^{-1}$	$4{\cdot}3212 \times 10^{0}$	$8{\cdot}1999 \times 10^{-1}$
$6{\cdot}0050 \times 10^{0}$	$6{\cdot}7732 \times 10^{-1}$	$2{\cdot}0338 \times 10^{0}$	$9{\cdot}6406 \times 10^{-1}$
$2{\cdot}1332 \times 10^{0}$	$9{\cdot}7656 \times 10^{-1}$	$1{\cdot}8995 \times 10^{0}$	$9{\cdot}7969 \times 10^{-1}$
$2{\cdot}3295 \times 10^{0}$	$9{\cdot}8906 \times 10^{-1}$	$2{\cdot}1651 \times 10^{0}$	$9{\cdot}9219 \times 10^{-1}$
$4{\cdot}9777 \times 10^{0}$	$9{\cdot}9844 \times 10^{-1}$	$4{\cdot}2622 \times 10^{0}$	$9{\cdot}9844 \times 10^{-1}$
$7{\cdot}4024 \times 10^{0}$	$2{\cdot}7850 \times 10^{-1}$	$1{\cdot}8995 \times 10^{0}$	$9{\cdot}7969 \times 10^{-1}$
$2{\cdot}1332 \times 10^{0}$	$9{\cdot}7656 \times 10^{1}$		
$7{\cdot}5941 \times 10^{0}$	$1{\cdot}9504 \times 10^{-1}$	$1{\cdot}2471 \times 10^{1}$	$1{\cdot}7028 \times 10^{-1}$
$8{\cdot}6787 \times 10^{0}$	$4{\cdot}5644 \times 10^{-1}$		

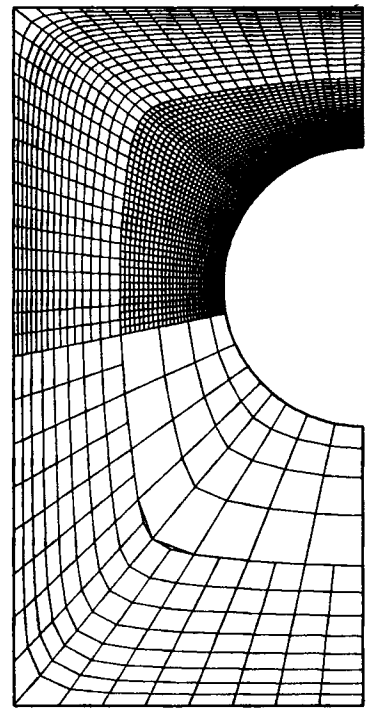

Figure 15. Segments of the first four grids used for case C4 (one-quarter of each)

(absolute residual sums less than 10^{-9} for $Pr=10$, and less than 10^{-8} for $Pr=0{\cdot}1$). The pure conduction heat transfer was solved first. Figure 16 shows the resulting isotherms. The total heat flux through the vertical cold wall and hot cylinder wall must be the same, since there is no heat transfer through the adiabatic horizontal walls and through the symmetry plane. In our calculations, this was ensured to seven most significant decimal places. Heat fluxes were, in this test case, normalized with the same normalization flux Q_N as in case C3. Thus, for the pure conduction heat transfer, a Nusselt number of 2·314 results (cf. Table VI).

Figure 17 shows the velocity vectors for the convection flow at $Ra=10^6$ and two Prandtl numbers: (a) $Pr=0{\cdot}1$ and (b) $Pr=10$. The corresponding streamlines are presented in Figure 18. Obviously, the Prandtl number has a large effect on the flow. Although in both cases, the Rayleigh number is the same, the Grashof number is larger for cases of smaller Prandtl number, since $Re=Gr\,Pr$. For the fluid parameters used here, the buoyancy source of momentum is the same in both cases, but the viscosity is an order of magnitude lower for $Pr=0{\cdot}1$. Therefore, velocities almost an order of magnitude higher than at $Pr=10$ result. Since the density is the same in both cases, the inertial forces will be significantly higher in the $Pr=0{\cdot}1$, case. In the case of $Pr=10$, the fluid starts leaving the cold wall and turning towards the hot cylinder already at half the height. At $Pr=0{\cdot}1$, this happens only after the bottom adiabatic wall is reached (cf. Figure 17). For the same reason, at $Pr=0{\cdot}1$, the hot fluid rising along the cylinder wall separates on the upper surface. Between the cylinder wall, symmetry plane and top adiabatic wall a weak eddy is formed which is attached to the main circuit at a free stagnation point (cf. Figure 18(a)). At $Pr=10$, the fluid remains attached to the hot cylinder the entire length (cf. Figure 18(b)).

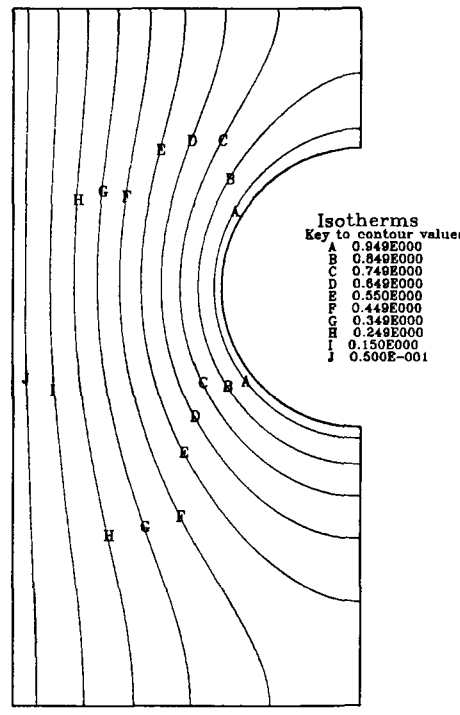

Figure 16. Isotherms of case C4 for pure conduction heat transfer

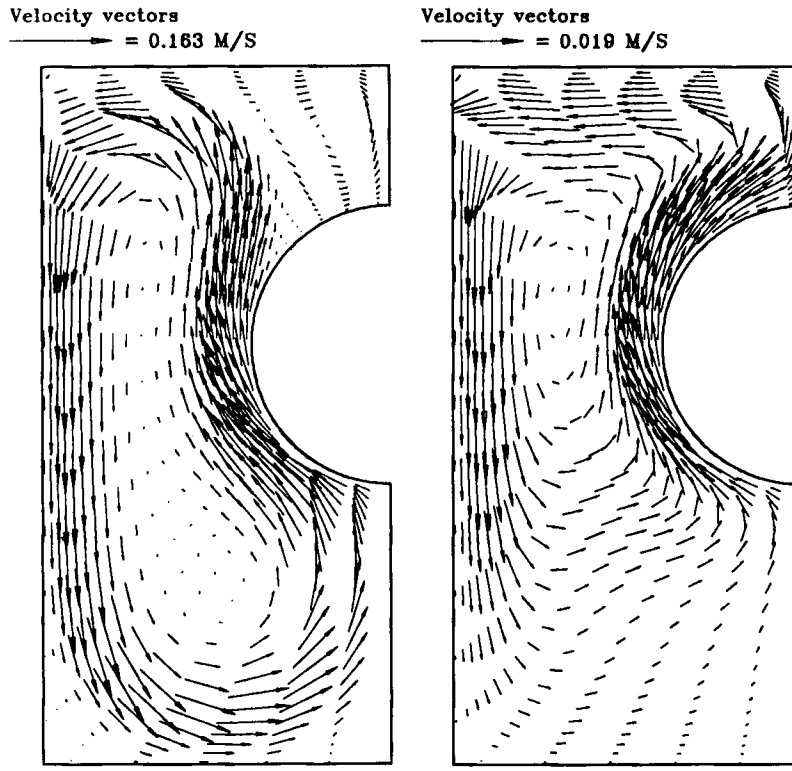

Figure 17. Predicted velocity vectors for case C4: (a) $Pr = 0{\cdot}1$; (b) $Pr = 10$

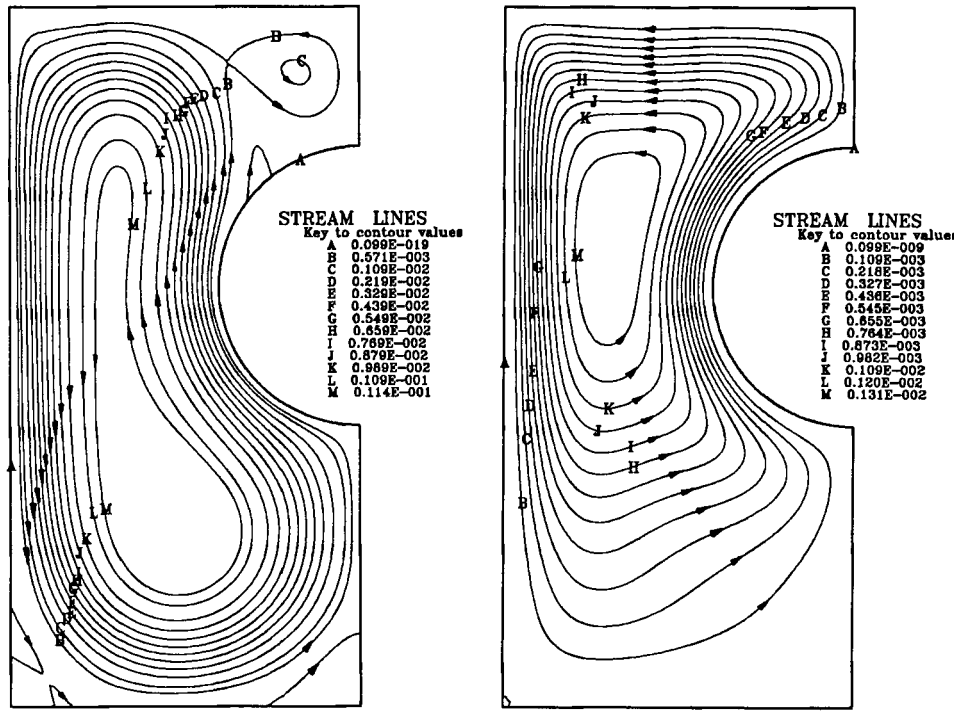

Figure 18. Predicted streamlines for case C4, 256 x 128 CV grid: (a) $Pr = 0{\cdot}1$; (b) $Pr = 10$

The total heat fluxes through the cold vertical wall and cylinder wall were again normalized with Q_N and presented in Table VI as $\overline{Nu}$. Also, the local heat flux maximum and minimum at the cold wall are shown, together with their position y^*. The isotherms for both Prandtl numbers are presented in Figure 19. A comparison with the isotherms for pure conduction (Figure 16) shows the effect of convection. Local Nusselt numbers along the cold vertical wall and cylinder wall, as predicted on the finest grid, are presented in Tables VIII and IX for $Pr = 0{\cdot}1$ and 10, respectively. Apart from the 15 characteristic values, the maxima are given as additional entries.

4. CONCLUSIONS

Four test problems involving fluid flow and heat transfer in geometries requiring the use of boundary-fitted, non-orthogonal grids were designed. They are suggested to be used for testing new numerical methods for heat and fluid flow and are accompanied with accurate reference solutions. The major conclusions from the present study may be summarized as follows:

1. Efficient finite volume multigrid methods are available for solving fluid flow and heat transfer problems in complex geometries involving a high degree of non-orthogonality. In one test case studied here the angle between grid lines was 30°.
2. Although the grid non-orthogonality and non-uniformity affect the magnitude of the truncation error on a given mesh, they do not prevent reduction of the discretization error by grid refinement. In all the cases studied here, which involve high non-orthogonality,

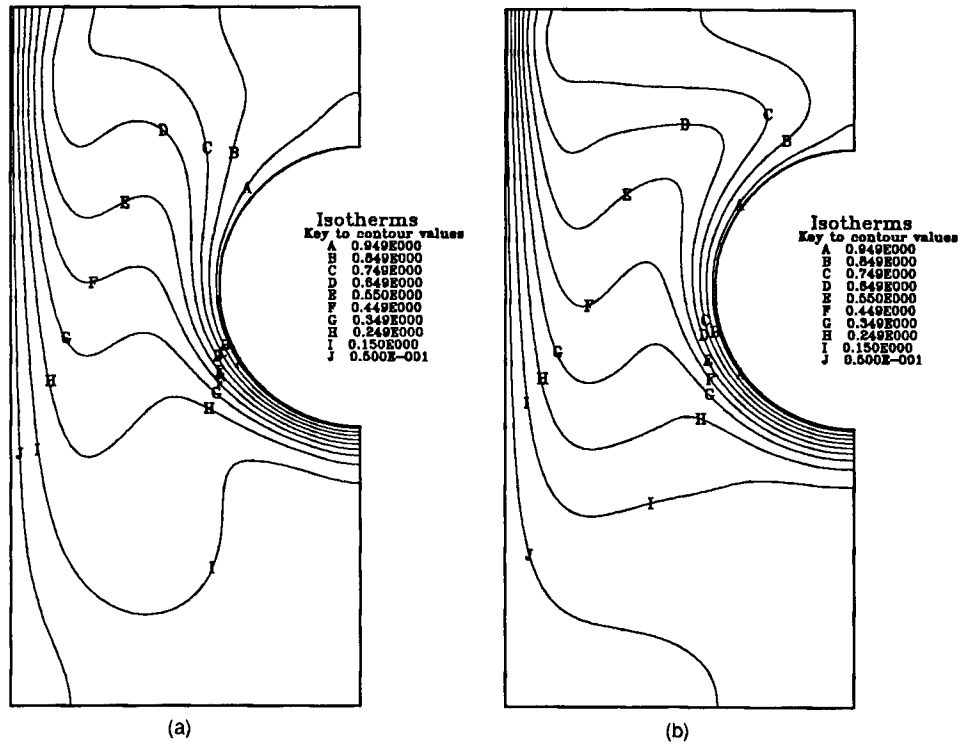

Figure 19. Predicted isotherms for case C4, 256 × 128 CV grid: (a) $Pr = 0{\cdot}1$; (b) $Pr = 10$

Table VIII. Selected values of the profiles of the local Nusselt number along the hot and cold walls for case C4 at $Pr=0{\cdot}1$ as predicted on the 256×128 CV grid

$Pr=0{\cdot}1$			
Nu_θ	θ	Nu_y	y
$2{\cdot}0142\times10^{1}$	$5{\cdot}0166\times10^{-1}$	$6{\cdot}4097\times10^{-1}$	$3{\cdot}9062\times10^{-3}$
$2{\cdot}0282\times10^{1}$	$4{\cdot}6500\times10^{0}$	$6{\cdot}7785\times10^{-1}$	$3{\cdot}5156\times10^{-2}$
$2{\cdot}1286\times10^{1}$	$1{\cdot}8771\times10^{1}$	$7{\cdot}6315\times10^{-1}$	$6{\cdot}6406\times10^{-2}$
$2{\cdot}1241\times10^{1}$	$2{\cdot}2934\times10^{1}$	$9{\cdot}0363\times10^{-1}$	$9{\cdot}7656\times10^{-2}$
$2{\cdot}0500\times10^{1}$	$3{\cdot}0519\times10^{1}$	$1{\cdot}1134\times10^{0}$	$1{\cdot}2891\times10^{-1}$
$1{\cdot}5842\times10^{1}$	$5{\cdot}4835\times10^{1}$	$1{\cdot}6551\times10^{0}$	$1{\cdot}8359\times10^{-1}$
$1{\cdot}4058\times10^{1}$	$6{\cdot}6010\times10^{1}$	$5{\cdot}4837\times10^{0}$	$4{\cdot}8047\times10^{-1}$
$1{\cdot}1355\times10^{1}$	$8{\cdot}6269\times10^{1}$	$7{\cdot}5666\times10^{0}$	$6{\cdot}0547\times10^{-1}$
$9{\cdot}6875\times10^{0}$	$9{\cdot}7336\times10^{1}$	$8{\cdot}7600\times10^{0}$	$6{\cdot}6016\times10^{-1}$
$4{\cdot}4214\times10^{0}$	$1{\cdot}2452\times10^{2}$	$1{\cdot}0954\times10^{1}$	$7{\cdot}3828\times10^{-1}$
$3{\cdot}4129\times10^{0}$	$1{\cdot}3140\times10^{2}$	$1{\cdot}3282\times10^{1}$	$8{\cdot}0859\times10^{-1}$
$2{\cdot}9059\times10^{0}$	$1{\cdot}3616\times10^{2}$	$1{\cdot}4389\times10^{1}$	$8{\cdot}5547\times10^{-1}$
$2{\cdot}2728\times10^{0}$	$1{\cdot}4546\times10^{2}$	$1{\cdot}4558\times10^{1}$	$8{\cdot}7891\times10^{-1}$
$9{\cdot}7626\times10^{-1}$	$1{\cdot}7396\times10^{2}$	$1{\cdot}4255\times10^{1}$	$9{\cdot}1016\times10^{-1}$
$8{\cdot}9660\times10^{-1}$	$1{\cdot}7923\times10^{2}$	$1{\cdot}2052\times10^{1}$	$9{\cdot}9609\times10^{-1}$
$2{\cdot}1300\times10^{1}$	$2{\cdot}0186\times10^{1}$	14558×10^{1}	$8{\cdot}7891\times10^{-1}$

Table IX. Selected values of the profiles of the local Nusselt number along the hot and cold walls for case C4 at $Pr=10$ as predicted on the 256×128 CV grid

$Pr=10$			
Nu_θ	θ	Nu_y	y
$1{\cdot}8592\times10^{1}$	$5{\cdot}0166\times10^{-1}$	$2{\cdot}5183\times10^{-1}$	$3{\cdot}9062\times10^{-3}$
$1{\cdot}8559\times10^{1}$	$6{\cdot}0643\times10^{0}$	$2{\cdot}6753\times10^{-1}$	$2{\cdot}7344\times10^{-2}$
$1{\cdot}8283\times10^{1}$	$1{\cdot}8054\times10^{1}$	$3{\cdot}0932\times10^{-1}$	$5{\cdot}0781\times10^{-2}$
$1{\cdot}7878\times10^{1}$	$2{\cdot}7543\times10^{1}$	$5{\cdot}8601\times10^{-1}$	$1{\cdot}1328\times10^{-1}$
$1{\cdot}7100\times10^{1}$	$4{\cdot}0170\times10^{1}$	$1{\cdot}0632\times10^{0}$	$1{\cdot}7578\times10^{-1}$
$1{\cdot}6041\times10^{1}$	$5{\cdot}3683\times10^{1}$	$1{\cdot}7164\times10^{0}$	$2{\cdot}3828\times10^{-1}$
$1{\cdot}5072\times10^{1}$	$6{\cdot}4477\times10^{1}$	$2{\cdot}5591\times10^{0}$	$3{\cdot}0078\times10^{-1}$
$1{\cdot}4181\times10^{1}$	$7{\cdot}3457\times10^{1}$	$6{\cdot}9512\times10^{0}$	$5{\cdot}5078\times10^{-1}$
$1{\cdot}2808\times10^{1}$	$8{\cdot}6269\times10^{1}$	$9{\cdot}6061\times10^{0}$	$6{\cdot}7578\times10^{-1}$
$6{\cdot}7174\times10^{0}$	$1{\cdot}4056\times10^{2}$	$1{\cdot}1521\times10^{1}$	$7{\cdot}4609\times10^{-1}$
$5{\cdot}4512\times10^{0}$	$1{\cdot}5104\times10^{2}$	$1{\cdot}3369\times10^{1}$	$8{\cdot}0078\times10^{-1}$
$4{\cdot}3752\times10^{0}$	$1{\cdot}5903\times10^{2}$	$1{\cdot}9523\times10^{1}$	$9{\cdot}4141\times10^{-1}$
$2{\cdot}2004\times10^{0}$	$1{\cdot}7287\times10^{2}$	$1{\cdot}9949\times10^{1}$	$9{\cdot}6484\times10^{-1}$
$1{\cdot}7557\times10^{0}$	$1{\cdot}7721\times10^{2}$	$1{\cdot}9915\times10^{1}$	$9{\cdot}7266\times10^{-1}$
$1{\cdot}6741\times10^{0}$	$1{\cdot}7923\times10^{2}$	$1{\cdot}8775\times10^{1}$	$9{\cdot}9609\times10^{-1}$
		$1{\cdot}9949\times10^{1}$	$9{\cdot}6484\times10^{-1}$

aspect ratios up to eight and moderate expansion ratios, the second-order convergence (error reduction by a factor of four), expected from central differencing, appears to prevail.

3. Convergence of the solution method is strongly influenced by the Reynolds, Rayleigh and Prandtl numbers, and much less by the grid non-orthogonality, aspect ratio and expansion

ratio. More iterations are needed as the Reynolds and Rayleigh numbers increase and the Prandtl number decreases.

4. The reference solutions presented here were obtained on fine grids of up to 320 × 320 control volumes. By comparing the solutions for grids with different fineness, the discretization errors were estimated to be of the order of 0·1% or less. The important features of the flow, e.g. vortex strength, centreline profiles, Nusselt numbers, etc., are presented in tabulated form to facilitate future comparisons. A proof of convergence towards a grid-independent solution is provided for most of these quantities.

It is believed that the test cases presented here could become standard problems for testing new numerical solution methods, both in terms of accuracy and efficiency.

ACKNOWLEDGEMENTS

The authors thank Dr.-Ing. G. Scheuerer and Dr.-Ing. R. Kessler for the useful discussions on the subject of this paper. The financial support from the Deutsche Forschungsgemeinschaft is greatly appreciated.

REFERENCES

1. U. Ghia, K. N. Ghia and C. T. Shin, 'High-*Re* solutions for incompressible flow using the Navier–Stokes equations and a multigrid method', *J. Comput. Phys.*, **48**, 387–411 (1982).
2. G. de Vahl Davis, 'Natural convection of air in a square cavity: a bench mark numerical solution', *Int. j. numer. methods fluids*, **3**, 249–264 (1983).
3. M. Hortmann, M. Perić and G. Scheuerer, 'Finite volume multigrid prediction of natural convection: bench-mark solutions', *Int. j. numer. methods fluids*, **11**, 189–207 (1990).
4. I. Demirdžić and M. Perić, 'Finite volume method for prediction of fluid flow in arbitrarily shaped domains with moving boundaries', *Int. j. numer. methods fluids*, **10**, 771–790 (1990).
5. M. Perić, R. Kessler and G. Scheuerer, 'Comparison of finite-volume numerical methods with staggered and collocated grids', *Comput. Fluids*, **16**, 389–403 (1988).
6. H. L. Stone, 'Iterative solution of implicit approximations of multi-dimensional partial differential equations', *SIAM J. Numer. Anal.*, **5**, 530–558 (1968).
7. S. V. Patankar and D. B. Spalding, 'A calculation procedure for heat, mass and momentum transfer in three-dimensional parabolic flows', *Int. J. Heat Mass Transfer*, **15**, 1787–1806 (1972).
8. M. Perić, 'A finite volume method for the prediction of three-dimensional flow in complex ducts', *Ph.D. Thesis*, University of London, 1985.
9. M. Perić, 'Analysis of pressure–velocity coupling on non-orthogonal grids', *Numer. Heat Transfer, Part B (Fundamentals)*, **17**, 63–82 (1990).
10. P. K. Khosla and S. G. Rubin, 'A diagonally dominant second-order accurate implicit scheme', *Comput. Fluids*, **2**, 207–209 (1974).
11. S. C. Caruso, J. H. Ferziger and J. Oliger, 'Adaptive grid techniques for elliptic problems', *Report TF-23*, Thermosciences Div., Stanford University, 1985.
12. K. C. Karki and S. V. Patankar, 'Calculation procedure for viscous incompressible flows in complex geometries', *Numer. Heat Transfer*, **14**, 295–307 (1988).
13. J. H. Ferziger, 'A note on numerical accuracy', *Int. j. numer. methods fluids*, **8**, 995–996 (1988).
14. J. F. Thompson, Z. U. A. Warsi and C. W. Mastin, *Numerical Grid Generation: Foundations and Applications*, North-Holland, New York, 1985.